

Jinhui Yan

Department of Civil and Environmental
Engineering,
University of Illinois at Urbana-Champaign,
205, N. Mathews Ave.,
Urbana, IL 61801
e-mail: yjh@illinois.edu

Xiaowei Deng

Department of Civil Engineering,
University of Hong Kong,
Pokfulam Road,
Hong Kong, 9990077, China
e-mail: xwdeng@hku.hk

Fei Xu

Ansys, Inc.,
807 Las Cimas Pkwy,
Austin, TX 78746
e-mail: fei.xu@ansys.com

Songzhe Xu

Department of Civil and Environmental
Engineering,
University of Illinois at Urbana-Champaign,
205, N. Mathews Ave.,
Urbana, IL 61801
e-mail: songzhex@sci.utah.edu

Qiming Zhu

Department of Civil and Environmental
Engineering,
University of Illinois at Urbana-Champaign,
205, N. Mathews Ave.,
Urbana, IL 61801
e-mail: qiming2@illinois.edu

Numerical Simulations of Two Back-To-Back Horizontal Axis Tidal Stream Turbines in Free-Surface Flows

We simulate two back-to-back full-scale tidal turbines using an in-house computational free-surface flow code. We briefly present the mathematical formulation of the computational framework. We first validate the proposed method on a single turbine configuration. A mesh refinement study is conducted to ensure the result is converged. We then quantify the wake effect and free-surface effect on tidal turbine performance by a case study. To investigate the free-surface effect, we perform both pure hydrodynamics and free-surface simulations. The time history of thrust and production coefficients is quantified. In both pure hydrodynamics and free-surface flow simulations, thrust and production coefficients of the downstream turbines drop significantly due to the velocity deficit in the wake. By comparing the result between free-surface flow and pure hydrodynamics simulations for the configuration considered here, we find that the free-surface does not affect the upstream turbine but significantly affects the downstream turbine. [DOI: 10.1115/1.4046317]

Keywords: computational mechanics, turbulence, free-surface flow, hydro energy

1 Introduction

Renewable energy is one of the important driving forces in reducing environmental pollution and greenhouse gas emission. Among many different kinds of renewable energy, the tidal energy that converts hydro-kinetic power to electricity has the potential to become a big source attributed to the predictability and repeatability of tidal power generation [1–5]. Compared with other tidal energy harvesting devices, horizontal axis tidal stream turbine (HATT) is the most developed one [6–9]. In the research around HATTs [10,11], tidal farm design and power generation are of the priority and attract the most attention. Therefore, accurate prediction of the hydrodynamic performance of tidal stream turbines is critical for the development of tidal energy, and numerous computational and experimental approaches have been proposed to achieve this goal [12–17]. Tidal energy can borrow many technologies from the wind energy industry because of the shared underlying mechanical principles. However, there are still several fundamental differences in the design, operation, and modeling between wind turbines and tidal stream turbines, such as different flow conditions, the free-surface effect, and possible occurrence of cavitation. In tidal farms, many tidal turbines are installed to extract maximum power. Due to the finite site of the tidal farm, flow interaction between turbines is very strong. The energy extracted by the downstream turbines is less than the upstream ones due to the negative wake effect, which

significantly reduces the overall power production of the entire tidal farm. Increasing the distance between turbines may reduce the wake effect. However, the availability of the site and the cost of electrical transmission, the availability of the site, and the electrical transmission cost constrain maximal distance. Although a considerable amount of research has focused on a single tidal turbine [12,18], it does not guarantee the optimal overall power generation of the entire tidal farm. Besides, HATTs operate in a bounded environment with limited available water depth, and the expansion of the wake is constrained by the free-surface. Thus, the modeling of the interaction between multiple tidal turbines subjected to realistic flow conditions, especially free-surface flow conditions, is critical but less investigated at this point. Traditionally, the blade element momentum method, vortex element method, and other reduced order numerical methods have been utilized in the tidal turbine design and the prediction of the turbine performance [13,19]. These methods are desirable in the optimization attributed to the low computational cost. But these methods rely on experimental measurements and empirical correlations to achieve accurate predictions. To our best knowledge, few considered the free-surface effect in their numerical simulations among these computational efforts, although experiments by Bahaj et al. [17,20] have quantitatively shown that free-surface can significantly affect the performance of tidal stream turbines.

The current paper presents numerical simulations of multiple HATTs at full-scale operating in realistic free-surface flows using a computational framework we proposed in Ref. [21]. In the computational framework, the level-set method [22–28] is utilized to track the evolution of the air–water interface. The unified two-phase Navier–Stokes equations of incompressible flows are employed to model the fluid motion. The fluid density and viscosity are

Contributed by the Applied Mechanics Division of ASME for publication in the JOURNAL OF APPLIED MECHANICS. Manuscript received January 9, 2020; final manuscript received February 6, 2020; published online February 12, 2020. Assoc. Editor: Yong-gang Huang.

interpolated by using the level-set function. The Arbitrary Lagrangian–Eulerian variational multi-scale (ALE–VMS) formulation enhanced with weak enforcement of essential boundary conditions with linear finite-element discretization is employed to solve the free-surface flow problems. The sliding-interface formulation is used to handle the relative motion between the rotating rotor and stationary tower, thus enabling the so-called “full-machine” simulation. The paper is outlined as follows. In Sec. 2, we introduce the governing equations of free-surface flows using the level-set method and two-phase Navier–Stokes equations at the continuous level. In Sec. 3, we present the major components of the computational formulation of free-surface flows at the space-discrete level, including ALE–VMS, weak enforcement of essential boundary conditions, and sliding interface technique. We also summarize other key numerical techniques, such as linearization, time integration, linear solver, re-distancing, and mass balancing of the level-set field, in this section. In Sec. 4, we first perform a mesh refinement study of a single turbine to validate the computational method. Then, we simulate two back-to-back HATTs using the proposed framework, which, to the best knowledge of the authors, is the first computational fluid dynamics (CFD) calculation of multiple tidal turbines in free-surface flows. Both pure hydrodynamics and free-surface flow simulations are performed with the same set of operation parameters, based on which the experimental measurement of a single turbine is available. We compare the performance between the upstream and downstream turbines and quantify the free-surface effect. In Sec. 5, we draw conclusions and specify future research.

2 Strong Form Equations of Free-Surface Flows

In this section, we summarize the strong-form governing equations of free-surface flows on a moving domain. Figure 1 shows a combined moving air–water domain with two back-to-back tidal turbines inside, denoted by $\Omega_t \in R^3$ at time t . Γ_t denotes its boundary. Ω_t^a , Ω_t^w , and Γ_t^{aw} denote the air subdomain, water subdomain, and air–water interface, respectively.

We employ the level-set method to simulate free-surface flows [22–26,29,30] around the tidal turbines. For this, a scalar function $\phi(\mathbf{x}, t)$ is defined in the fluid domain. $\phi(\mathbf{x}, t)$ is the signed distance of \mathbf{x} with respect to the air–water interface, and its zero level ($\phi(\mathbf{x}, t) = 0$) defines the air–water interface and divides the spatial fluid domain into air subdomain Ω_t^a and water subdomain Ω_t^w , which are defined by

$$\Omega_t^a = \{\mathbf{x} | \phi(\mathbf{x}, t) < 0, \forall \mathbf{x} \in \Omega_t\} \quad (1)$$

$$\Omega_t^w = \{\mathbf{x} | \phi(\mathbf{x}, t) > 0, \forall \mathbf{x} \in \Omega_t\} \quad (2)$$

$$\Gamma_t^{aw} = \{\mathbf{x} | \phi(\mathbf{x}, t) = 0, \forall \mathbf{x} \in \Omega_t\} \quad (3)$$

The flow motion is governed by the Navier–Stokes equations of incompressible flows posed on a moving domain by Arbitrary Lagrangian–Eulerian (ALE) description, which reads

$$\rho \left(\frac{\partial \mathbf{u}}{\partial t} \Big|_{\hat{\mathbf{x}}} + (\mathbf{u} - \hat{\mathbf{u}}) \cdot \nabla_{\mathbf{x}} \mathbf{u} - \mathbf{g} \right) + \nabla p - \mu \Delta_{\mathbf{x}} \mathbf{u} = \mathbf{0} \quad (4)$$

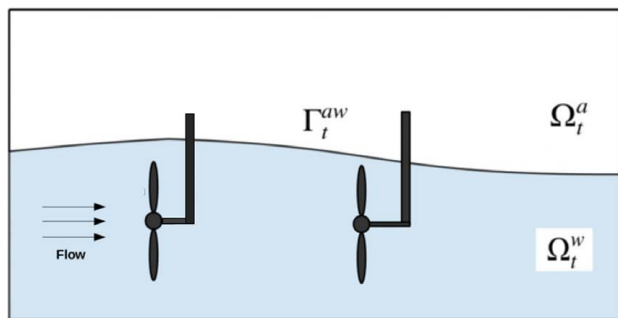


Fig. 1 The fluid spatial domain with air and water subdomains separated by the free-surface

$$\nabla_{\mathbf{x}} \cdot \mathbf{u} = 0 \quad (5)$$

where \mathbf{u} and p are the fluid velocity and pressure, \mathbf{g} is the gravitational acceleration vector, $\hat{\mathbf{u}}$ is the velocity of the fluid domain, $\Delta_{\mathbf{x}}$ is the Laplace operator, and $\nabla_{\mathbf{x}}$ is the gradient operator. In the above Navier–Stokes equations, the partial time derivative of the velocity field is taken holding the referential configuration (denoted by $\hat{\mathbf{x}}$) fixed, and the space derivatives are taken with respect to the current configuration denoted by \mathbf{x} . In the ALE formulation, the fluid domain velocity $\hat{\mathbf{u}}$ is completely independent of the fluid particle velocity \mathbf{u} , which allows users to choose any mesh motion scheme that is convenient for the problem.

At each point of the two-phase fluid domain, the fluid density ρ and dynamic viscosity μ in Eq. (4) will be assigned the corresponding values by the following interpolation.

$$\rho = \rho_w H_c(\phi) + \rho_a (1 - H_c(\phi)) \quad (6)$$

$$\mu = \mu_w H_c(\phi) + \mu_a (1 - H_c(\phi)) \quad (7)$$

where $H_c(\phi)$ is the regularized Heaviside function defined by Eq. (8), ρ_a , μ_a , ρ_w , and μ_w are the density and dynamic viscosity of air and water, respectively.

$$H_c(\phi) = \begin{cases} 0 & \text{if } \phi < -\epsilon \\ \frac{1}{2} \left(1 + \frac{\phi}{\epsilon} + \sin\left(\frac{\phi\pi}{\epsilon}\right) \right) & \text{if } |\phi| \leq \epsilon \\ 1 & \text{if } \phi > \epsilon \end{cases} \quad (8)$$

In Eq. (8), ϵ defines a finite width of the air–water interface. In a numerical setting, ϵ scales with the local mesh element length. The air–water interface is moving with the fluid material particles, which is modeled by a pure convection equation of the level-set field. In the ALE description, the equation reads

$$\frac{\partial \phi}{\partial t} \Big|_{\hat{\mathbf{x}}} + (\mathbf{u} - \hat{\mathbf{u}}) \cdot \nabla_{\mathbf{x}} \phi = 0 \quad (9)$$

Similarly, the time derivative is taken holding the referential configuration fixed, and the spatial derivative is taken with respect to the current configuration. Together with the appropriate initial and boundary conditions, Eqs. (4)–(9) formulate a complete model of free-surface flows of tidal turbines on a moving domain.

3 Numerical Methods

In this section, we show the numerical method for solving the above free-surface flow equations. We present the Arbitrary Lagrangian–Eulerian variational multi-scale (ALE–VMS), weak enforcement of essential boundary conditions, and sliding interface technique with details. Other numerical techniques, including linearization, re-distancing, linear solvers, and time integration, are briefly summarized.

3.1 ALE–VMS Formulation With Weak Enforcement of Essential Boundary Conditions. The Reynolds number of the free-surface flows around tidal turbines is very high. To handle the turbulence, we utilize the ALE–VMS formulation [31,32], which has been successfully applied to a variety of challenging high Reynolds number CFD and fluid–structure interaction (FSI) problems in wind energy and marine engineering [33–40], to attain the space-discrete version of the free-surface flow equations. For that, let \mathcal{V}^h denote the discrete trial set for the velocity–pressure–level-set triple $\{\mathbf{u}^h, p^h, \phi^h\}$ and let \mathcal{W}^h be the discrete test set for the linear momentum, continuity and level-set convection equations $\{\mathbf{w}^h, q^h, \eta^h\}$. The ALE–VMS formulation of free-surface flows is stated as follows: Find $\{\mathbf{u}^h, p^h, \phi^h\} \in \mathcal{V}^h$ such that $\forall \{\mathbf{w}^h, q^h, \eta^h\} \in \mathcal{W}^h$,

$$B^{ALE-VMS}(\{\mathbf{w}^h, q^h, \eta^h\}, \{\mathbf{u}^h, p^h, \phi^h\}) - F^{ALE-VMS}(\mathbf{w}^h, q^h, \eta^h) = 0 \quad (10)$$

where $B^{ALE-VMS}$ and $F^{ALE-VMS}$ are given by

$$\begin{aligned}
 & B^{ALE-VMS}(\{\mathbf{w}^h, q^h, \eta^h\}, \{\mathbf{u}^h, p^h, \phi^h\}) \\
 &= \left(\mathbf{w}^h, \rho \frac{\partial \mathbf{u}}{\partial t} \Big|_{\hat{\mathbf{x}}} + \rho(\mathbf{u}^h - \hat{\mathbf{u}}^h) \cdot \nabla_{\mathbf{x}} \mathbf{u}^h \right)_{\Omega_i} + (\nabla_{\mathbf{x}} \mathbf{w}^h, -p\mathbf{I} + 2\mu \nabla_{\mathbf{x}}^s \mathbf{u})_{\Omega_i} \\
 &+ (q^h, \nabla_{\mathbf{x}} \cdot \mathbf{u}^h)_{\Omega_i} + \sum_{e=1}^{Nel} \left(\tau_M(\mathbf{u}^h - \hat{\mathbf{u}}^h) \cdot \nabla_{\mathbf{x}} \mathbf{w}^h + \tau_M \frac{\nabla_{\mathbf{x}} q^h}{\rho}, \mathbf{r}_M(\mathbf{u}^h, p^h) \right)_{\Omega_i^e} \\
 &+ \sum_{e=1}^{Nel} (\rho \tau_C \nabla_{\mathbf{x}} \cdot \mathbf{w}^h, r_C(\mathbf{u}^h, p^h))_{\Omega_i^e} - \sum_{e=1}^{Nel} (\tau_M \mathbf{w}^h, \mathbf{r}_M(\mathbf{u}^h, p^h) \cdot \nabla_{\mathbf{x}} \mathbf{u}^h)_{\Omega_i^e} \\
 &- \sum_{e=1}^{Nel} \left(\frac{\nabla_{\mathbf{x}} \mathbf{w}^h}{\rho} : \tau_M \mathbf{r}_M(\mathbf{u}^h, p^h) \otimes \tau_M \mathbf{r}_M(\mathbf{u}^h, p^h) \right)_{\Omega_i^e} \\
 &+ \sum_{e=1}^{Nel} \left(\eta^h, \frac{\partial \phi^h}{\partial t} \Big|_{\hat{\mathbf{x}}} + (\mathbf{u}^h - \hat{\mathbf{u}}^h) \cdot \nabla_{\mathbf{x}} \phi^h \right)_{\Omega_i^e} + \sum_{e=1}^{Nel} (\tau_{\phi}(\mathbf{u}^h - \hat{\mathbf{u}}^h) \cdot \nabla_{\mathbf{x}} \eta^h, r_L(\mathbf{u}^h, \phi^h))_{\Omega_i^e}
 \end{aligned} \tag{11}$$

and

$$F^{ALE-VMS}(\mathbf{w}^h, q^h, \eta^h) = (\mathbf{w}^h, \rho \mathbf{g})_{\Omega_i} + (\mathbf{w}^h, \mathbf{h})_{\Gamma_i^h} \tag{12}$$

where $\nabla_{\mathbf{x}}^s$ is the symmetric gradient operator, \mathbf{h} is the prescribed traction vector on the Neumann-type boundary Γ_i^h . In the above equation, the operator $(\mathbf{X}_1, \mathbf{X}_2)_A$ denotes the L_2 -inner product of \mathbf{X}_1 and \mathbf{X}_2 over the domain A . The terms integrated over element interiors may be interpreted as the stabilized method for fluid mechanics, where N_{el} is the number of elements, τ_M , τ_C , and τ_{ϕ} are the corresponding stabilization parameters [41–43]. These terms also act as a large Eddy simulation turbulence model for high Reynolds number wall bounded flows. $\mathbf{r}_M(\mathbf{u}^h, p^h)$, $r_C(\mathbf{u}^h, p^h)$ and $r_L(\mathbf{u}^h, \phi^h)$ are the strong-form linear momentum, continuity, and level-set convection equation residuals, respectively, given as

$$\mathbf{r}_M(\mathbf{u}^h, p^h) = \rho \left(\frac{\partial \mathbf{u}^h}{\partial t} \Big|_{\hat{\mathbf{x}}} + (\mathbf{u}^h - \hat{\mathbf{u}}^h) \cdot \nabla_{\mathbf{x}} \mathbf{u}^h - \mathbf{g} \right) + \nabla p^h - 2\mu \Delta_{\mathbf{x}} \mathbf{u}^h \tag{13}$$

$$r_C(\mathbf{u}^h) = \nabla_{\mathbf{x}} \cdot \mathbf{u}^h \tag{14}$$

$$r_L(\mathbf{u}^h, \phi^h) = \frac{\partial \phi^h}{\partial t} \Big|_{\hat{\mathbf{x}}} + (\mathbf{u}^h - \hat{\mathbf{u}}^h) \cdot \nabla_{\mathbf{x}} \phi^h \tag{15}$$

For large-scale, high Reynolds number wall-bounded flows, fully resolving of viscous turbulent boundary layers is nearly impossible. To relax the requirement of boundary layers resolution without sacrificing the accuracy of hydrodynamic loading on the tidal turbine, another crucial ingredient needed to be included in the formulation is the weak enforcement of essential boundary conditions (weak BCs). For this, several additional terms acting on the fluid-turbine interface are added to Eq. (10), and the semi-discrete problem becomes: Find $\{\mathbf{u}^h, p^h, \phi^h\} \in \mathcal{V}^h$ such that $\forall \{\mathbf{w}^h, q^h, \eta^h\} \in \mathcal{W}^h$,

$$\begin{aligned}
 & B^{ALE-VMS}(\{\mathbf{w}^h, q^h, \eta^h\}, \{\mathbf{u}^h, p^h, \phi^h\}) - F^{ALE-VMS}(\mathbf{w}^h, q^h, \eta^h) \\
 &- \sum_{b=1}^{N_{eb}} (\mathbf{w}^h, \boldsymbol{\sigma}(\mathbf{u}^h, p^h) \mathbf{n})_{\Gamma_i^b \cap \Gamma_i^g} - \sum_{b=1}^{N_{eb}} (2\mu(\nabla_{\mathbf{x}}^s \mathbf{w}^h) \mathbf{n} + q^h \mathbf{n}, \mathbf{u}^h - \mathbf{v}^h)_{\Gamma_i^b \cap \Gamma_i^g} \\
 &- \sum_{b=1}^{N_{eb}} (\mathbf{w}^h, (\rho \mathbf{u}^h \cdot \mathbf{n} - \rho \hat{\mathbf{u}}^h \cdot \mathbf{n})(\mathbf{u}^h - \mathbf{v}^h))_{\Gamma_i^b \cap \Gamma_i^g} \\
 &+ \sum_{b=1}^{N_{eb}} (\tau_B \mathbf{w}^h, \mathbf{u}^h - \mathbf{v}^h)_{\Gamma_i^b \cap \Gamma_i^g} = 0
 \end{aligned} \tag{16}$$

where \mathbf{v}^h is the prescribed velocity (determined by the rotational speed of the rotor in the current case) on the fluid-turbine interface denoted by Γ_i^g . \mathbf{n} is the unit normal vector on Γ_i^g . Γ_i^g is decomposed

into N_{eb} surfaces denoted with Γ_i^b . $(\Gamma_i^g)^-$ is the inflow part of Γ_i^g , given as $(\Gamma_i^g)^- = \{\mathbf{x} \mid \mathbf{u}^h \cdot \mathbf{n} < 0, \forall \mathbf{x} \in \Gamma_i^g\}$. τ_B is a penalty parameter chosen for the balance of accuracy and stability of the numerical formulation. Compared with the strongly enforced essential boundary conditions (strong BCs) approach, in which the nodal value at the boundary is replaced by the prescribed boundary value, the weak BCs add more flexibility by allowing the flow to slightly slip on the tidal turbine surface in the case when the mesh size in wall-normal direction is relatively coarse. This technique tends to produce more accurate results than those coming from strong BCs when the boundary layer mesh is not sufficiently fine to completely resolve the detailed turbulent boundary layers. Readers are referred to Refs. [44–54] for more details on weak BCs and their successful applications to wind turbine CFD and FSI simulations. The comparison of performance between weak BCs and strong BCs in the context of ALE-VMS for the simulations of a NASA Ames 80 ft × 120 ft wind turbine can be found in Ref. [55].

3.2 Sliding Interface Formulation for Objects in Relative Motion. “Full machine” simulations need to handle the relative motion between the stationary tower and the rotating rotor. For that, we employ the sliding interface technique that utilizes a stationary subdomain for the tower and a rotating subdomain for the rotor (see Fig. 2). The two domains share a sliding cylindrical interface and are in relative motion, resulting in non-matching meshes on each side of the interface. The sliding interface

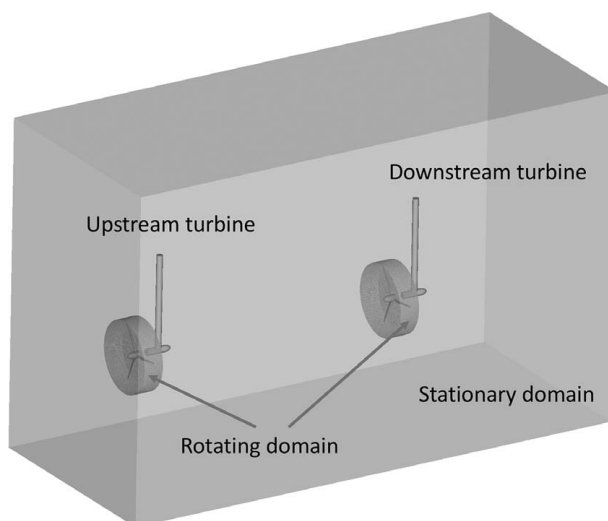


Fig. 2 Fluid mechanics domain and sliding interface

technique imposes the continuity constraints of the kinematics and traction at the interface between the stationary and rotating subdomains. Such a technique was originally developed in Ref. [56] for simulating fluid flows around rotating components and has been applied to many CFD and FSI simulation with structures in relative motion [35,49,57]. The technique is extended to take the continuity of the level-set function into consideration in Ref. [21] to simulate free-surface flows. To present some details of the method, let the subscripts s and m denote the quantities associated with the fluid mechanics problem on the stationary and moving subdomains, respectively. To enforce the continuity of the flow kinematics, traction, and level-set function at the sliding interface, we add the following terms to the left-hand side of Eq. (16)

$$\begin{aligned}
& - \sum_{b=1}^{Neb} \left(\frac{1}{2} (\mathbf{w}_s^h - \mathbf{w}_m^h), \boldsymbol{\sigma}_s \mathbf{n}_s - \boldsymbol{\sigma}_m \mathbf{n}_m \right)_{\Gamma_i^b \cap \Gamma_i^{st}} \\
& - \sum_{b=1}^{Neb} \left(\frac{1}{2} (\delta \boldsymbol{\sigma}_s \mathbf{n}_s - \delta \boldsymbol{\sigma}_m \mathbf{n}_m), \mathbf{u}_s^h - \mathbf{u}_m^h \right)_{\Gamma_i^b \cap \Gamma_i^{st}} \\
& - \sum_{b=1}^{Neb} (\mathbf{w}_s^h, \rho [(\mathbf{u}_s^h - \hat{\mathbf{u}}_s^h) \cdot \mathbf{n}_s]_- (\mathbf{u}_s^h - \mathbf{u}_m^h))_{\Gamma_i^b \cap \Gamma_i^{st}} \\
& - \sum_{b=1}^{Neb} (\mathbf{w}_m^h, \rho [(\mathbf{u}_m^h - \hat{\mathbf{u}}_m^h) \cdot \mathbf{n}_m]_- (\mathbf{u}_m^h - \mathbf{u}_s^h))_{\Gamma_i^b \cap \Gamma_i^{st}} \quad (17) \\
& + \sum_{b=1}^{Neb} (\lambda_B (\mathbf{w}_s^h - \mathbf{w}_m^h), \mathbf{u}_s^h - \mathbf{u}_m^h)_{\Gamma_i^b \cap \Gamma_i^{st}} \\
& - \sum_{b=1}^{Neb} (\eta_s^h [(\mathbf{u}_s^h - \hat{\mathbf{u}}_s^h) \cdot \mathbf{n}_s]_-, \phi_s^h - \phi_m^h)_{\Gamma_i^b \cap \Gamma_i^{st}} \\
& - \sum_{b=1}^{Neb} (\eta_m^h [(\mathbf{u}_m^h - \hat{\mathbf{u}}_m^h) \cdot \mathbf{n}_m]_-, \phi_m^h - \phi_s^h)_{\Gamma_i^b \cap \Gamma_i^{st}}
\end{aligned}$$

where Γ_i^{st} denotes the sliding interface, \mathbf{n}_s and \mathbf{n}_m are the unit normal vectors of the interface, $\boldsymbol{\sigma}$ and $\delta \boldsymbol{\sigma}$ are the Cauchy stress tensor and its variation, given as $\boldsymbol{\sigma} = -p\mathbf{I} + 2\mu \nabla^s \mathbf{u}$ and $\delta \boldsymbol{\sigma} = 2\mu \nabla^s (\mathbf{w}^h) \mathbf{n} + q^h \mathbf{n}$, respectively. The operator $[A]_-$ denotes the negative part of A , which is $[A]_- = A$ if $A < 0$ and $[A]_- = 0$ if $A > 0$. λ_B is a penalty parameter chosen for the balance of accuracy and stability of the numerical formulation. The sliding interface formulation is derived from a discontinuous Galerkin method, where the basis function is continuous everywhere in the interior of the two-fluid subdomains except the sliding interface. In the present work, the fluid subdomain that encloses the turbine tower is stationary, thus $\hat{\mathbf{u}}_s^h = 0$. However, the formulation is capable of handling situations where both subdomains are in motion with arbitrary sliding interface shape between them. The simulation of two compliant hydrofoils in a tandem configuration is such an example, which can be found in Ref. [57].

3.3 Other Numerical Details. In the present work, linear finite elements are used for the spatial discretization, and the generalized- α method [58] is employed for time integration. A two-stage predictor-corrector algorithm based on Newton's method is used to solve the nonlinear equations. At each Newton iteration, a flexible GMRES algorithm is employed to solve the fluid velocity, pressure, and level-set increments simultaneously. The flexible GMRES solver is preconditioned using the iterative solution of individual linearized Navier–Stokes, and level-set equations, as proposed in Ref. [26]. Besides, to ensure the signed property of the level-set function and global mass conservation, the re-distancing and mass balancing processes of the level-set field are performed at the end of each time-step.

4 Free-Surface Simulations of Two Back-to-Back Tidal Turbines

4.1 Tidal Turbine Rotor Geometry. The geometry of the tidal turbine used in this paper is the same as that used in our previous single turbine simulations [21]. The turbine rotor, which was originally designed by Ref. [17], is widely used for validating numerical simulations for tidal energy, because of the availability of experimental data characterizing its hydrodynamic performance in free-surface flows [17,20]. The tidal turbine rotor has three blades with a diameter of $D=0.8$ m and 20 deg hub-pitch angle. Each blade is composed of NACA 63-812, NACA 63-815, NACA 63-818, NACA 63-821, and NACA 63-824 airfoil cross section shapes. The 3D rotor blades are constructed by stacking the appropriately scaled, offset, and twisted 2D cross sections.

4.2 Method Validation. To validate the method, we perform a refinement study of a single-tidal turbine in free-surface flow using a deep-immersion case, of which the experimental measurement of thrust coefficient and production coefficient is obtained in Refs. [17,20]. The computational domain is a box with dimensions $5 \text{ m} \times 2.8 \text{ m} \times 2.64 \text{ m}$ ($6.25D \times 3.5D \times 3.3D$). An initial study has been conducted to ensure that the computational domain is big enough to avoid the side wall effect. Figure 3 shows a snapshot of the computational domain. We design two refined regions to better capture the wake and free-surface evolution. The volumetric mesh makes use of triangular prisms in the rotor boundary layers and tetrahedra elsewhere. Two meshes with different element lengths are utilized. Figure 4 shows a plane cut of the coarse mesh. Tables 1 and 2 summarize the statistics of the two meshes.

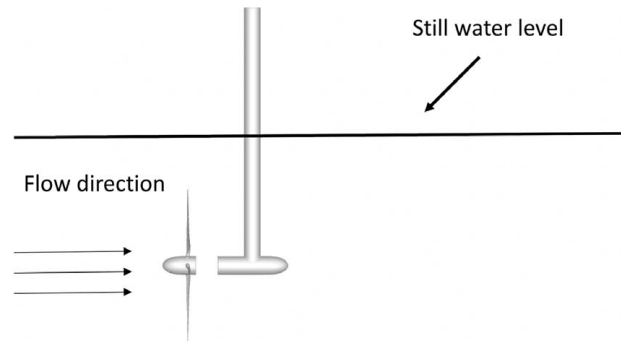


Fig. 3 Problem set-up and computational domain of the single turbine simulation

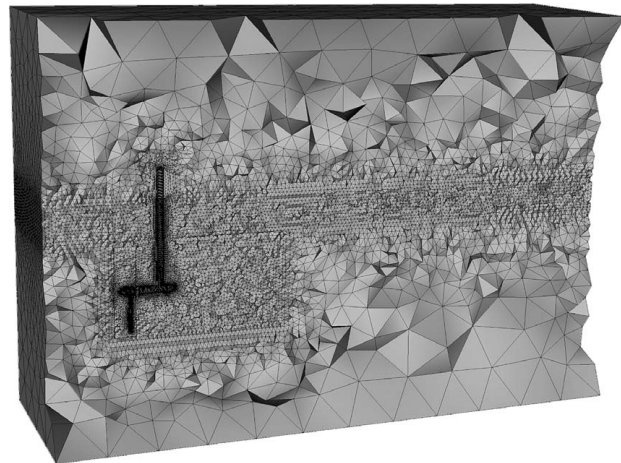


Fig. 4 A snapshot of the coarse mesh of the single turbine simulation on a planar cut ($y=0$)

Table 1 Element length (in meters) of the meshes of the single turbine simulations

| Mesher | Refined region (wake) | Refined region (free-surface) | Rotor boundary layer |
|--------|-----------------------|-------------------------------|----------------------|
| Fine | 0.03 | 0.03 | 0.0005 |
| Coarse | 0.06 | 0.06 | 0.001 |

Table 2 Mesh statistics of the single turbine simulations

| Mesher | Number of nodes | Number of elements |
|--------|-----------------|--------------------|
| Fine | 1,351,490 | 7,800,145 |
| Coarse | 503,611 | 2,874,939 |

The operation parameters are set as follows. The rotor speed is set to $\Omega = 28.250$ rad/s, water speed is set to $U_0 = 1.5$ m/s, and the tip immersion of $0.75D$ is used (the deep-immersion case in Refs. [17,20,21]). The boundary conditions are set as follows. Zero wind speed is applied strongly on the air portion of the inlet,

and the desired uniform water speed is applied strongly on the water portion of the inlet; the level-set field is also prescribed strongly on the inlet boundary as a linear function of the vertical coordinate. The top and outlet surfaces are set to the hydrostatic pressure boundary conditions; no penetration boundary condition is applied on two lateral surfaces and the bottom surface. The time-step is set to $\Delta t = 1 \times 10^{-4}$ s.

Figure 5 shows the time history of the thrust and production coefficients, which are defined as $C_T = 4T/0.5\rho_w\pi D^2 U_0^2$ and $C_P = 4Q\Omega/0.5\rho_w\pi D^2 U_0^3$ (T and Q are the thrust and torque, respectively). The experimental data from Refs. [17,20] are also plotted for comparison. Figure 6 shows the free-surface deformation and tip vortex contours colored by velocity magnitude at the fully developed stage. Although the coarse mesh slightly underestimates the coefficients and loses some flow features of the vortex structure, reasonable accuracy is obtained for both meshes. In order to achieve better accuracy, the element lengths based on the fine mesh will be used in the next two back-to-back turbines simulation.

4.3 Simulations of Two Back-to-Back Tidal Turbines. One important fact, which was observed in both the experiment [17,20] and our previous computation of a single turbine [21], is that the thrust and production coefficients are higher in the deep-immersion

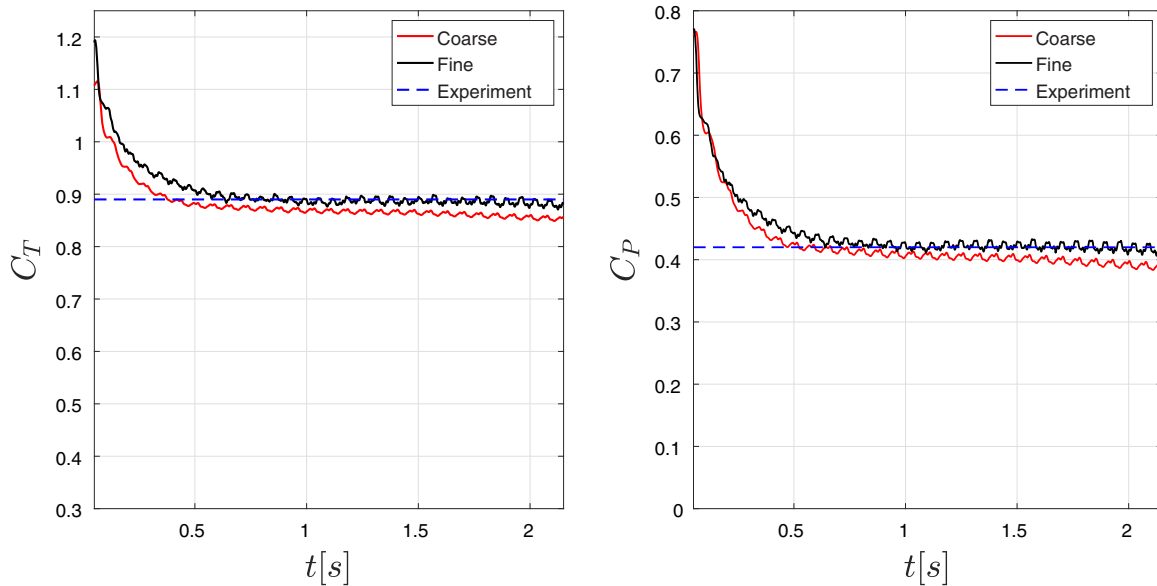


Fig. 5 Thrust and production coefficients of a single turbine: refinement study

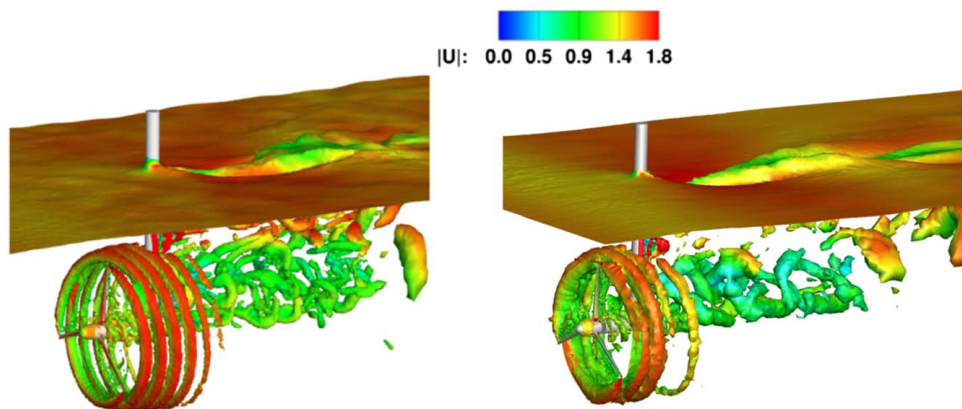


Fig. 6 Snapshots of air–water interface and underwater vorticity colored by velocity magnitude (in m/s) of a single turbine ($t = 1.8$ s): refinement study (left: fine mesh. right: coarse mesh)

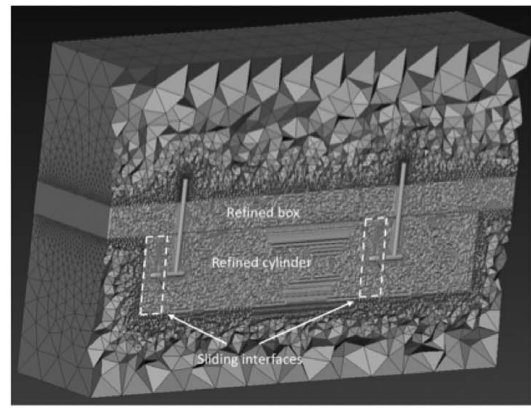
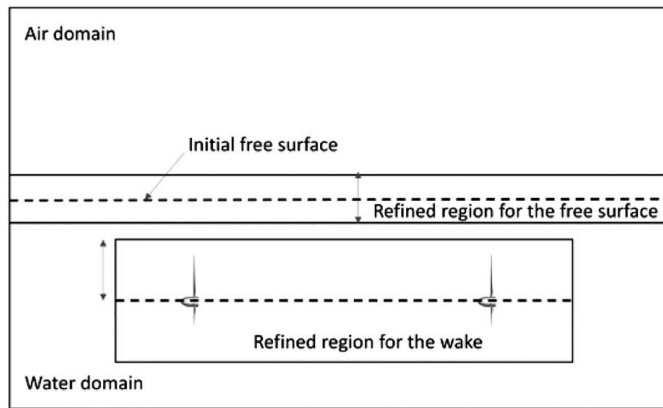


Fig. 7 Left: Problem setup of two back to back turbines (Turbine towers are removed for illustration purpose.). Right: A 2D cut to show the mesh quality used in the two back-to-back simulation. Two refined regions are built to better capture the turbulent wake and free-surface evolution.

Table 3 Element length (in meters) of the mesh of the two back-to-back simulation

| Outer box | Refined region (wake) | Refined region (free-surface) | Rotor boundary layer |
|-----------|-----------------------|-------------------------------|----------------------|
| 0.5 | 0.03 | 0.03 | 0.0005 |

Table 4 Mesh statistics of the two back-to-back simulations

| Number of nodes | Number of elements |
|-----------------|--------------------|
| 1,351,490 | 7,800,145 |

case than those in the shallow-immersion case. In the deep-immersion case, the free-surface effect is negligible. As a result, pure hydrodynamics and free-surface simulations give quite similar predictions for thrust and production coefficients. But the free-surface effect is significant for the shallow-immersion case by decreasing the thrust and production coefficients.

Based on our previous work in Ref. [21], we present the simulation of two back-to-back tidal turbines. The deep-immersion case from the experiment in Refs. [17,20] is chosen. The goal is trying to answer the following two questions: (1) How much is the efficiency drop of the downstream turbine? (2) Is the free-surface effect still important for this two back-to-back turbine configuration, given the fact that the free-surface effect is not important for a single turbine with this immersion depth? To quantify the free-surface effect, we perform both pure hydrodynamics and free-surface simulations.

The same operation parameters of the single turbine simulation [21] are utilized. The distance between the upstream turbine and downstream turbine is $L = 3.5$ m. The computational domain of the free-surface simulation is a box with dimensions $6.5 \text{ m} \times 2.8 \text{ m} \times 2.64 \text{ m}$ ($8.125D \times 3.5D \times 3.3D$). Similar to the mesh used in the validation section, we design a refined cylinder and a refined box around the still water level to better capture the turbulent wake generated by the upstream turbine and the free-surface evolution. Figure 7 shows the problem setup and a snapshot of the mesh on a planar cut. The domain is divided into three subdomains separated by two cylinder-shaped sliding interfaces.

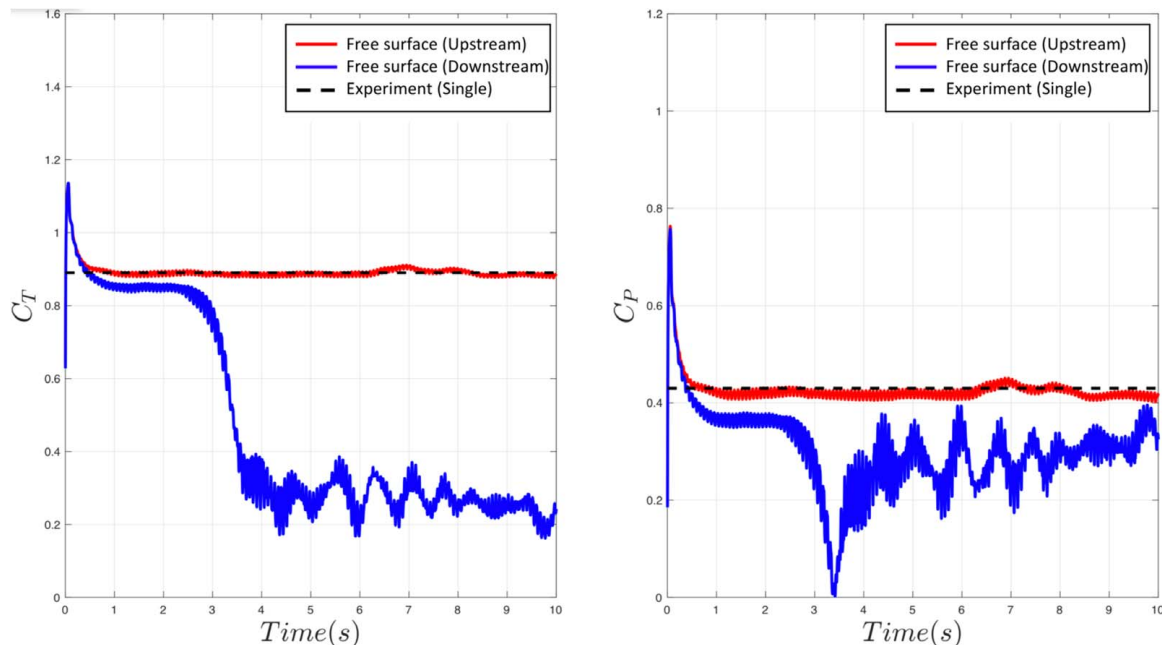


Fig. 8 Time history of thrust and production coefficients predicted by the free-surface flow simulation

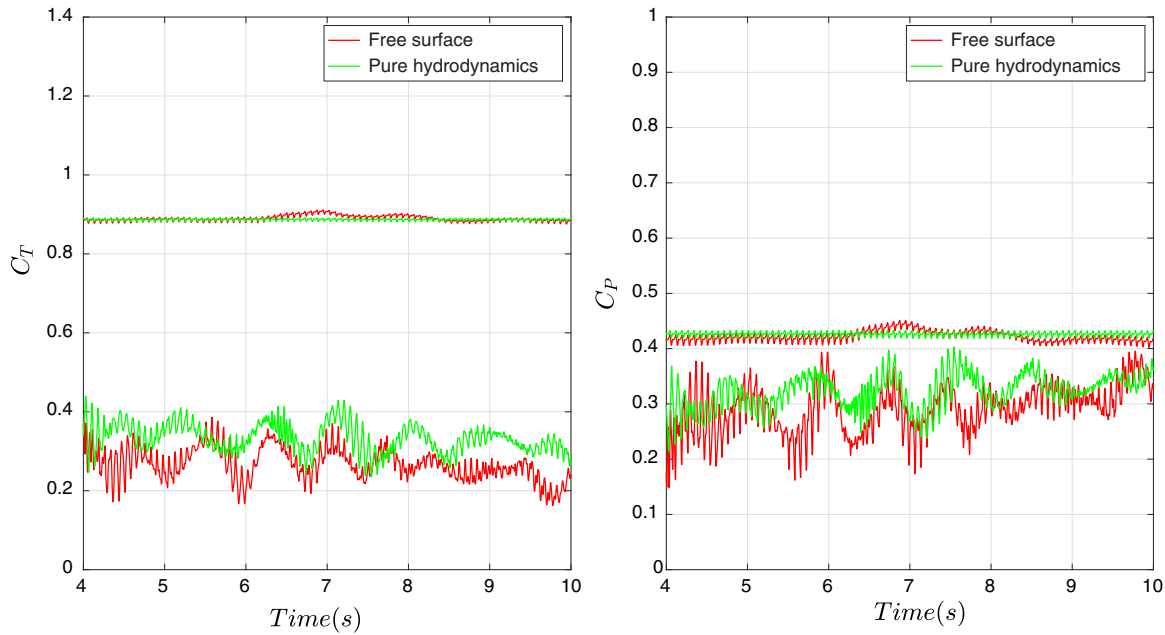


Fig. 9 Thrust and production coefficients predicted by the pure hydrodynamics and free-surface flow simulations in fully developed stage

Table 5 Average thrust and production coefficients

| Cases | \bar{C}_T | \bar{C}_P |
|---|-------------|-------------|
| Free-surface (upstream turbine) | 0.8894 | 0.4216 |
| Pure hydrodynamics (upstream turbine) | 0.8902 | 0.4263 |
| Free-surface (downstream turbine) | 0.2698 | 0.2886 |
| Pure hydrodynamics (downstream turbine) | 0.2886 | 0.3308 |

Table 3 shows the element length employed, and Table 4 shows the total number of nodes and elements. We use the same mesh in the pure hydrodynamics simulation to eliminate the influence of the mesh on the results. For the free-surface simulation, the boundary conditions are the same as the single turbine simulation. For pure hydrodynamics simulation, uniform water speed is applied strongly everywhere on the inlet; zero traction boundary condition is adopted for the outlet; no penetration boundary condition is used for other

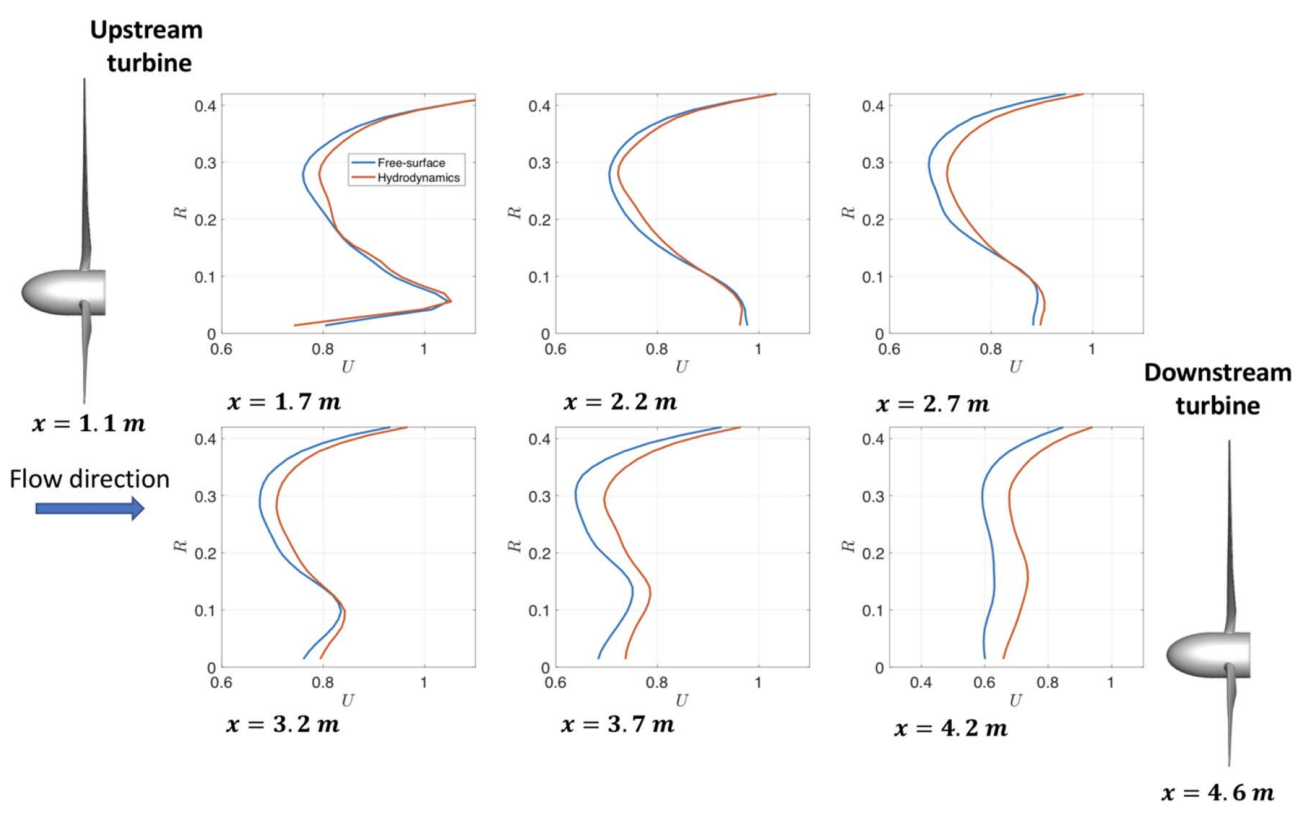


Fig. 10 Water speed between the two turbines averaged over 10 rotor revolutions plotted at different locations as a function of the radial coordinate

surfaces. The time-step is set to $\Delta t = 1 \times 10^{-4}$ s for both free-surface and pure hydrodynamics simulations.

Figure 8 shows the predicted time history of C_T and C_P of the upstream turbine and the downstream turbine from the free-surface simulation. The results are compared with the experimental data of a single turbine with the same immersion depth from Ref. [17]. We see the coefficients of the upstream turbine still stay at the same level with the single turbine configuration, the thrust coefficient, and the production coefficient of the downstream turbine are only 30% and 62.3% of that of the single turbine. Higher-amplitude fluctuations of C_T and C_P of the downstream turbine are also observed.

Figure 9 shows the comparison between the pure hydrodynamics and the free-surface simulations for C_T and C_P prediction in the fully developed stage. Table 5 summarizes the averaged coefficients from 4 s to 10 s. For the upstream turbine, the averaged thrust and production coefficients predicted by the pure hydrodynamics and the free-surface flow simulations are quite similar, still agreeing with experimental data based on a single turbine from Ref. [17], which indicates that the free-surface still does not affect the upstream turbine performance in this deep-immersion case. But, for the downstream turbine, the pure hydrodynamics simulation predicts higher coefficients than the free-surface flow simulation. The discrepancy is 7% for the thrust coefficient and 15% for the production coefficient, respectively.

Figure 10 shows the water speed at different locations between the two turbines averaged over 10 rotor revolutions as a function of the radial coordinate. A short distance past the upstream turbine, the velocity deviates from a uniform profile. As going downstream, the average water speed gradually decreases. We also observe that the averaged water speed at a specified radial coordinate is lower in the free-surface flow simulation, which explains the smaller prediction of thrust and production coefficients. These findings indicate that the free-surface does not affect the upstream tidal turbine but significantly change the performance of the downstream turbine in the current turbine arrangement.

Figure 11 shows the vorticity colored by velocity magnitude for the pure hydrodynamics simulation at the fully developed stage. A large amount of tip vortex is generated in the wake due to the rotation of the upstream turbine rotor. The turbulent wake causes the high amplitude fluctuations of C_T and C_P seen in Figs. 8 and 9. From these visualizations, we also see that the solution fields are quite continuous across the non-matching sliding interface, which indicates that the sliding-interface technique is successful for handling this type of problem involving components in relative motions.

Figure 12 shows the vorticity and deformed free-surface colored by the velocity magnitude at $t=0.025$ s, 2.1 s, 9.4 s, and 10.8 s of the free-surface simulation. Significant topological changes of the

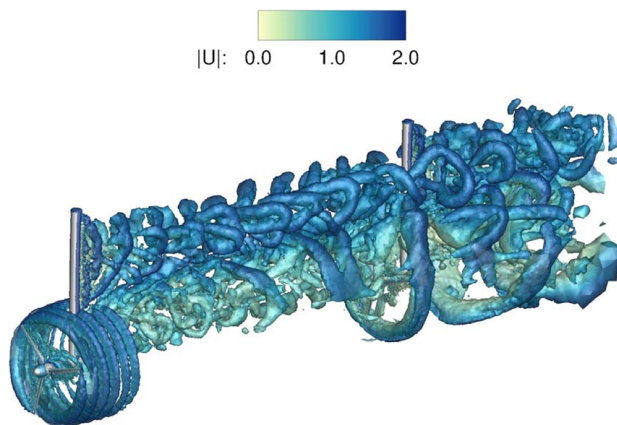


Fig. 11 Pure hydrodynamics simulation. Vorticity colored by velocity magnitude (in m/s).

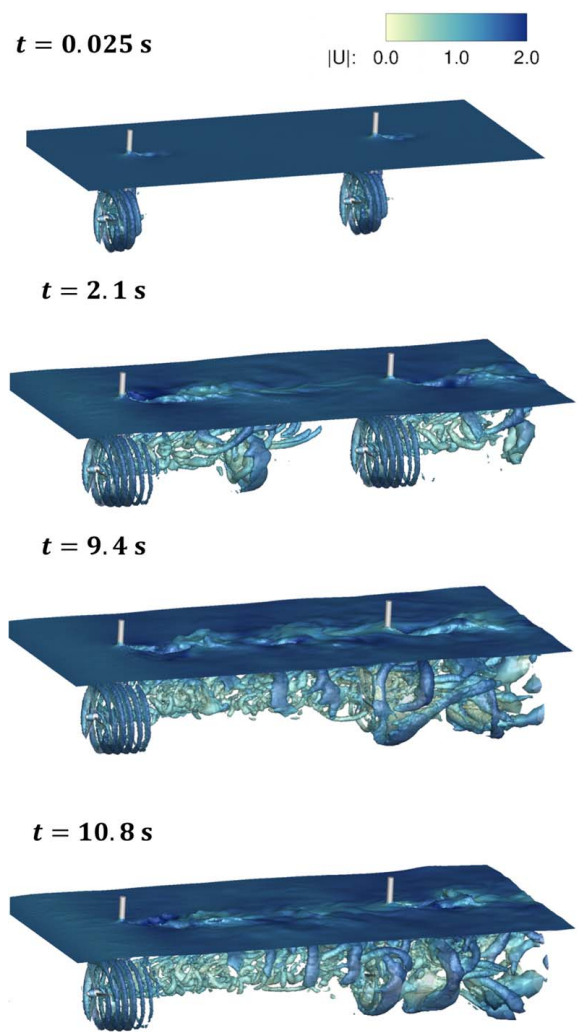


Fig. 12 Free-surface and underwater vorticity colored by the velocity magnitude (in m/s)

air–water interface are observed after the flow hit the tower of the upstream turbine. Before the wake hits the downstream turbine, the vorticity structure of both turbines can maintain six tube-like vortex structures. However, after the turbulent wake reaches the downstream turbine, these tubes of the downstream turbine break and form big vortices. As going downstream, we observe that the interaction between tip vortex and free-surface becomes more and more pronounced, resulting in substantial the air–water interface deformation, which consequently produces a more pronounced free-surface effect on the thrust and production coefficients of the downstream turbine.

5 Conclusions and Future Research

We simulated two back-to-back tidal turbines using a computational free-surface flow formulation. The simulations are carried out at full-scale and with the full complexity of tidal turbine geometry. Without any empiricism, the simulations can accurately capture the effect of the free-surface on the rotor hydrodynamic loading and interaction between the upstream and downstream turbines.

For the deep-immersion operating conditions considered in the present work, a drop in thrust coefficient of 70% and a drop of production coefficient in 38.7% between the upstream and downstream turbines were predicted by the free-surface simulation. By comparing the results of the pure hydrodynamics simulation and free-surface simulation, we found that the free-surface does not affect

the upstream turbine but significantly change the performance of the downstream turbine for this deep-immersion case.

This work is a first step of using free-surface flow simulations of multiple full-scale tidal turbines to understand the combined wake and free-surface effects on these machines and to improve the efficiency of tidal farms with finite sites. In the future, the parametric study of the distance between the upstream turbine and downstream turbine will be performed. We also plan to extend the current methodology to simulate multiple tidal turbines arranged in arrays. Regarding method development, fluid–structure interaction (FSI) effect and cavitation will be considered in future research.

Acknowledgment

The first author is partially supported by the ASME Robert M. and Mary Haythornthwaite Research Initiation Award and a seed grant from the Institute for Sustainability, Energy, and Environment at the University of Illinois at Urbana-Champaign. The simulations were performed at the Texas Advanced Supercomputing Center. These supports are gratefully acknowledged.

References

- [1] Burrows, R., Yates, N. C., Hedges, T. S., Li, M., Zhou, J., Chen, D., Walkington, I., Wolf, J., Holt, J., and Proctor, R., 2009, “Tidal Energy Potential in UK Waters,” Proceedings of the Institution of Civil Engineers—Maritime Engineering, London, Vol. 162, Thomas Telford Ltd., pp. 155–164.
- [2] Ponta, F. L., and Jacovkis, P. M., 2008, “Marine-Current Power Generation by Diffuser-Augmented Floating Hydro-Turbines,” *Renewable Energy*, **33**(4), pp. 665–673.
- [3] Brutto, O. A. L., Guillou, S. S., Thiébot, J., and Gualous, H., 2017, “Assessing the Effectiveness of a Global Optimum Strategy Within a Tidal Farm for Power Maximization,” *Appl. Energy*, **204**, pp. 653–666.
- [4] Ward, S. L., Robins, P. E., Lewis, M. J., Iglesias, G., Hashemi, M. R., and Neill, S. P., 2018, “Tidal Stream Resource Characterisation in Progressive Versus Standing Wave Systems,” *Appl. Energy*, **220**, pp. 274–285.
- [5] Barbarelli, S., Florio, G., Amelio, M., and Scornaienchi, N., 2018, “Preliminary Performance Assessment of a Novel On-Shore System Recovering Energy From Tidal Currents,” *Appl. Energy*, **224**, pp. 717–730.
- [6] Goundar, J. N., and Ahmed, M. R., 2013, “Design of a Horizontal Axis Tidal Current Turbine,” *Appl. Energy*, **111**, pp. 161–174.
- [7] Chen, Y., Lin, B., Lin, J., and Wang, S., 2017, “Experimental Study of Wake Structure Behind a Horizontal Axis Tidal Stream Turbine,” *Appl. Energy*, **196**, pp. 82–96.
- [8] Lee, J. H., Park, S., Kim, D. H., Rhee, S. H., and Kim, M. C., 2012, “Computational Methods for Performance Analysis of Horizontal Axis Tidal Stream Turbines,” *Appl. Energy*, **98**, pp. 512–523.
- [9] Liu, P., and Bose, N., 2012, “Prototyping a Series of Bi-Directional Horizontal Axis Tidal Turbines for Optimum Energy Conversion,” *Appl. Energy*, **99**, pp. 50–66.
- [10] Kolekar, N., and Banerjee, A., 2015, “Performance Characterization and Placement of a Marine Hydrokinetic Turbine in a Tidal Channel Under Boundary Proximity and Blockage Effects,” *Appl. Energy*, **148**, pp. 121–133.
- [11] Brutto, O. A. L., Thiébot, J., Guillou, S. S., and Gualous, H., 2016, “A Semi-Analytic Method to Optimize Tidal Farm Layouts—Application to the Alderney Race (raz Blanchard), France,” *Appl. Energy*, **183**, pp. 1168–1180.
- [12] Batten, W. M. J., Bahaj, A. S., Molland, A. F., and Chaplin, J. R., 2006, “Hydrodynamics of Marine Current Turbines,” *Renewable Energy*, **31**(2), pp. 249–256.
- [13] Batten, W. M. J., Bahaj, A. S., Molland, A. F., and Chaplin, J. R., 2008, “The Prediction of the Hydrodynamic Performance of Marine Current Turbines,” *Renewable Energy*, **33**(5), pp. 1085–1096.
- [14] Batten, W. M. J., Bahaj, A. S., Molland, A. F., and Chaplin, J. R., and Sustainable Energy Research Group, 2007, “Experimentally Validated Numerical Method for the Hydrodynamic Design of Horizontal Axis Tidal Turbines,” *Ocean Eng.*, **34**(7), pp. 1013–1020.
- [15] Bahaj, A. S., and Myers, L. E., 2003, “Fundamentals Applicable to the Utilisation of Marine Current Turbines for Energy Production,” *Renewable Energy*, **28**(14), pp. 2205–2211.
- [16] Bai, X., Avital, E. J., Munjiza, A., and Williams, J. J., 2014, “Numerical Simulation of a Marine Current Turbine in Free Surface Flow,” *Renewable Energy*, **63**, pp. 715–723.
- [17] Bahaj, A. S., Molland, A. F., Chaplin, J. R., and Batten, W. M. J., 2007, “Power and Thrust Measurements of Marine Current Turbines Under Various Hydrodynamic Flow Conditions in a Cavitation Tunnel and a Towing Tank,” *Renewable Energy*, **32**(3), pp. 407–426.
- [18] Zhu, Q., and Yan, J., 2019, “A Moving-Domain CFD Solver in Fenics With Applications to Tidal Turbine Simulations in Turbulent Flows,” *Comput. Math. Appl.* in press.

- [19] Clarke, J. A., Connor, G., Grant, A. D., and Johnstone, C. M., 2007, “Design and Testing of a Contra-Rotating Tidal Current Turbine,” *Proc. Inst. Mech. Eng., Part A: J. Power Energy*, **221**(2), pp. 171–179.
- [20] Bahaj, A. S., Batten, W. M. J., and McCann, G., 2007, “Experimental Verifications of Numerical Predictions for the Hydrodynamic Performance of Horizontal Axis Marine Current Turbines,” *Renewable Energy*, **32**(15), pp. 2479–2490.
- [21] Yan, J., Deng, X., Korobenko, A., and Bazilevs, Y., 2017, “Free-Surface Flow Modeling and Simulation of Horizontal-Axis Tidal-Stream Turbines,” *Comput. Fluids*, **158**, pp. 157–166.
- [22] Osher, S., and Sethian, J. A., 1988, “Fronts Propagating With Curvature-Dependent Speed: Algorithms Based on Hamilton-Jacobi Formulations,” *J. Comput. Phys.*, **79**(1), pp. 12–49.
- [23] Osher, S., and Fedkiw, R., 2006, *Level Set Methods and Dynamic Implicit Surfaces*, Vol. 153, Springer Science and Business Media.
- [24] Akkerman, I., Bazilevs, Y., Kees, C. E., and Farthing, M. W., 2011, “Isogeometric Analysis of Free-Surface Flow,” *J. Comput. Phys.*, **230**, pp. 4137–4152.
- [25] Akkerman, I., Bazilevs, Y., Benson, D. J., Farthing, M. W., and Kees, C. E., 2012, “Free-Surface Flow and Fluid–Object Interaction Modeling With Emphasis on Ship Hydrodynamics,” *ASME J. Appl. Mech.*, **79**(1), p. 010905.
- [26] Yan, J., Korobenko, A., Deng, X., and Bazilevs, Y., 2016, “Computational Free-Surface Fluid–Structure Interaction With Application to Floating Offshore Wind Turbines,” *Comput. Fluids*, **141**(1), pp. 155–174.
- [27] Kees, C. E., Akkerman, I., Farthing, M. W., and Bazilevs, Y., 2011, “A Conservative Level Set Method Suitable for Variable-Order Approximations and Unstructured Meshes,” *J. Comput. Phys.*, **230**, pp. 4536–4558.
- [28] Zhu, Q., Xu, F., Xu, S., Hsu, M.-C., and Yan, J., 2019, “An Immersogeometric Formulation for Free-Surface Flows With Application to Marine Engineering Problems,” *Comput. Methods Appl. Mech. Eng.*, **361**(1), pp. 112748–112798.
- [29] Yan, J., Yan, W., Lin, S., and Wagner, G. J., 2018, “A Fully Coupled Finite Element Formulation for Liquid–Solid–Gas Thermo-Fluid Flow With Melting and Solidification,” *Comput. Methods Appl. Mech. Eng.*, **336**, pp. 444–470.
- [30] Yan, J., Lin, S., Bazilevs, Y., and Wagner, G. J., 2018, “Isogeometric Analysis of Multi-Phase Flows With Surface Tension and with Application to Dynamics of Rising Bubbles,” *Comput. Fluids*, **179**, pp. 777–789.
- [31] Bazilevs, Y., Hsu, M.-C., Takizawa, K., and Tezduyar, T. E., 2012, “ALE-VMS and ST-VMS Methods for Computer Modeling of Wind-Turbine Rotor Aerodynamics and Fluid–Structure Interaction,” *Math. Models Methods Appl. Sci.*, **22**(supp02), p. 1230002.
- [32] Takizawa, K., Bazilevs, Y., Tezduyar, T. E., Long, C. C., Marsden, A. L., and Schjodt, K., 2014, “ST and ALE-VMS Methods for Patient-Specific Cardiovascular Fluid Mechanics Modeling,” *Math. Models Methods Appl. Sci.*, **24**, pp. 2437–2486.
- [33] Bazilevs, Y., Korobenko, A., Deng, X., Yan, J., Kinzel, M., and Dabiri, J. O., 2014, “FSI Modeling of Vertical-Axis Wind Turbines,” *ASME J. Appl. Mech.*, **81**(1), p. 081006.
- [34] Bazilevs, Y., Korobenko, A., Yan, J., Pal, A., Gohari, S. M. I., and Sarkar, S., 2015, “ALE-VMS Formulation for Stratified Turbulent Incompressible Flows with Applications,” *Math. Models Methods Appl. Sci.*, **25**(1), p. 1540011.
- [35] Bazilevs, Y., Korobenko, A., Deng, X., and Yan, J., 2015, “Novel Structural Modeling and Mesh Moving Techniques for Advanced FSI Simulation of Wind Turbines,” *Int. J. Numerical Methods Eng.*, **102**(3–4), pp. 766–783.
- [36] Korobenko, A., Hsu, M.-C., Akkerman, I., and Bazilevs, Y., 2013, “Aerodynamic Simulation of Vertical-Axis Wind Turbines,” *ASME J. Appl. Mech.*, **81**(1), p. 021011.
- [37] Korobenko, A., Yan, J., Gohari, S., Sarkar, S., and Bazilevs, Y., 2017, “Fsi Simulation of Two Back-To-Back Wind Turbines in Atmospheric Boundary Layer Flow,” *Comput. Fluids*, **158**, pp. 167–175.
- [38] Korobenko, A., Hsu, M.-C., Akkerman, I., Tippmann, J., and Bazilevs, Y., 2013, “Structural Mechanics Modeling and FSI Simulation of Wind Turbines,” *Math. Models Methods Appl. Sci.*, **23**(2), pp. 249–272.
- [39] Ravensbergen, M., Bayram, A., and Korobenko, A., 2020, “The Actuator Line Method for Wind Turbine Modelling Applied in a Variational Multiscale Framework,” *Comput. Fluids*, p. 104465.
- [40] Bayram, A., Bear, C., Bear, M., and Korobenko, A., 2020, “Performance Analysis of Two Vertical-Axis Hydrokinetic Turbines Using Variational Multiscale Method,” *Comput. Fluids*, **200**, pp. 104432.
- [41] Brooks, A. N., and Hughes, T. J. R., 1982, “Streamline Upwind/Petrov-Galerkin Formulations for Convection Dominated Flows With Particular Emphasis on the Incompressible Navier-Stokes Equations,” *Comput. Methods Appl. Mech. Eng.*, **32**(1–3), pp. 199–259.
- [42] Tezduyar, T. E., 2003, “Computation of Moving Boundaries and Interfaces and Stabilization Parameters,” *Int. J. Numerical Methods Fluids*, **43**(5), pp. 555–575.
- [43] Takizawa, K., Tezduyar, T. E., and Kuraishi, T., 2015, “Multiscale ST Methods for Thermo-Fluid Analysis of a Ground Vehicle and Its Tires,” *Math. Models Methods Appl. Sci.*, **25**(12), pp. 2227–2255.
- [44] Bazilevs, Y., and Hughes, T. J. R., 2007, “Weak Imposition of Dirichlet Boundary Conditions in Fluid Mechanics,” *Comput. Fluids*, **36**(1), pp. 12–26.
- [45] Bazilevs, Y., Michler, C., Calo, V. M., and Hughes, T. J. R., 2010, “Isogeometric Variational Multiscale Modeling of Wall-Bounded Turbulent Flows With Weakly Enforced Boundary Conditions on Unstretched Meshes,” *Comput. Methods Appl. Mech. Eng.*, **199**(13–16), pp. 780–790.
- [46] Takizawa, K., Tezduyar, T. E., Mochizuki, H., Hattori, H., Mei, S., Pan, L., and Montel, K., 2015, “Space-Time VMS Method for Flow Computations with Slip Interfaces (ST-SI),” *Math. Models Methods Appl. Sci.*, **25**(12), pp. 2377–2406.

- [47] Takizawa, K., Tezduyar, T. E., Kuraishi, T., Tabata, S., and Takagi, H., 2016, "Computational Thermo-Fluid Analysis of a Disk Brake," *Comput. Mech.*, **57**(6), pp. 965–977. Published online, doi:10.1007/s00466-016-1272-4
- [48] Hsu, M.-C., Akkerman, I., and Bazilevs, Y., 2014, "Finite Element Simulation of Wind Turbine Aerodynamics: Validation Study Using NREL Phase VI Experiment," *Wind Energy*, **17**(3), pp. 461–481.
- [49] Hsu, M.-C., and Bazilevs, Y., 2012, "Fluid–Structure Interaction Modeling of Wind Turbines: Simulating the Full Machine," *Comput. Mech.*, **50**(6), pp. 821–833.
- [50] Xu, F., Schillinger, D., Kamensky, D., Varduhn, V., Wang, C., and Hsu, M.-C., 2016, "The Tetrahedral Finite Cell Method for Fluids: Immersogeometric Analysis of Turbulent Flow Around Complex Geometries," *Comput. Fluids*, **141**, pp. 135–154.
- [51] Wang, C., Xu, F., Hsu, M.-C., and Krishnamurthy, A., 2017, "Rapid B-Rep Model Preprocessing for Immersogeometric Analysis Using Analytic Surfaces," *Comput. Aided Geometric Des.*, **52–53**, pp. 190–204.
- [52] Bazilevs, Y., Kamran, K., Moutsanidis, G., Benson, D., and Oñate, E., 2017, "A New Formulation for Air-Blast Fluid–Structure Interaction Using An Immersed Approach. Part I: Basic Methodology and FEM-Based Simulations," *Comput. Mech.*, **60**(1), pp. 83–100.
- [53] Bazilevs, Y., Moutsanidis, G., Bueno, J., Kamran, K., Kamensky, D., Hillman, M. C., Gomez, H., and Chen, J., 2017, "A New Formulation for Air-Blast Fluid–Structure Interaction Using An Immersed Approach: Part II—Coupling of IGA and Meshfree Discretizations," *Comput. Mech.*, **60**(1), pp. 101–116.
- [54] Xu, F., Moutsanidis, G., Kamensky, D., Hsu, M.-C., Murugan, M., Ghoshal, A., and Bazilevs, Y., 2017, "Compressible Flows on Moving Domains: Stabilized Methods, Weakly Enforced Essential Boundary Conditions, Sliding Interfaces, and Application to Gas-Turbine Modeling," *Comput. Fluids*, **158**, pp. 201–220.
- [55] Hsu, M.-C., Akkerman, I., and Bazilevs, Y., 2012, "Wind Turbine Aerodynamics Using ALE–VMS: Validation and the Role of Weakly Enforced Boundary Conditions," *Comput. Mech.*, **50**(4), pp. 499–511.
- [56] Bazilevs, Y., and Hughes, T. J. R., 2008, "NURBS-Based Isogeometric Analysis for the Computation of Flows About Rotating Components," *Comput. Mech.*, **43**(1), pp. 143–150.
- [57] Yan, J., Augier, B., Korobenko, A., Czarnowski, J., Ketterman, G., and Bazilevs, Y., 2015, "FSI Modeling of a Propulsion System Based on Compliant Hydrofoils in a Tandem Configuration," *Comput. Fluids*, **141**, pp. 201–211.
- [58] Chung, J., and Hulbert, G. M., 1993, "A Time Integration Algorithm for Structural Dynamics With Improved Numerical Dissipation: The Generalized- α Method," *ASME J. Appl. Mech.*, **60**(2), pp. 371–375.